Hindawi
Journal of Engineering
Volume 2019, Article ID 1862917, 13 pages
https://doi.org/10.1155/2019/1862917

Research Article

Analysis of Hybrid Ejector Absorption Cooling System

Doniazed Sioud and Ahmed Bellagi

Department of Energy Engineering, Ecole Nationale d'Ingénieurs de Monastir (ENIM), University of Monastir, Tunisia

Correspondence should be addressed to Doniazed Sioud; siouddoniazed@gmail.com

Received 17 July 2018; Revised 25 February 2019; Accepted 17 March 2019; Published 2 September 2019

Academic Editor: Oronzio Manca

Copyright © 2019 Doniazed Sioud and Ahmed Bellagi. This is an open access article distributed under the Creative Commons Attribution License, which permits unrestricted use, distribution, and reproduction in any medium, provided the original work is properly cited.

In this paper, a hybrid ejector single-effect lithium-bromide water cycle is theoretically investigated. The system is a conventional single-effect cycle activated by an external steam-ejector loop. A mathematical model of the whole system is developed. Simulations are carried out to study the effect of the major parameters of the hybrid cycle on its performances and in comparison with the conventional cycle. The ejector performance is also investigated. Results show that the entrainment ratio rises with steam pressure and condenser temperature, while it decreases with increasing generator temperature. The effect of the evaporator temperature on ejector performance is negligible. It is shown also that the hybrid cycle exhibits better performances than the corresponding basic cycle. However, the performance improvement is limited to a specific range of the operating parameters. Outside this range, the hybrid system behaves similar to a conventional cycle. Inside this range, the *COP* increases, reaches a maximum, and then decreases and rejoins the behavior of the basic cycle. The maximum *COP*, which can be as large as that of a conventional double-effect cycle, about 1, is obtained at lower temperatures than in the case of single-effect cycles.

1. Introduction

Cooling and air conditioning are essential for small scale and large industrial process applications. While systems applying the vapor-compression technique use environmental harmful refrigerants (FCC, FCHC, etc.), absorption technique for production of cold is based on environment friendly working fluids, namely, aqueous lithium bromide solutions with water as refrigerant or water-ammonia mixtures with ammonia as refrigerant. This technique however suffers from low performances. That is the reason why new hybrid and combined configurations are proposed, implying the integration of new components, particularly ejectors, in order to enhance the performances.

Various configurations incorporating ejectors were studied. Exhaustive review of the literature on this subject can be found in Besagni *et al*. [1, 2]. Elaborated CFD-models of ejectors developed to evaluate the ejector performances in both on-design and off-design conditions have been also published [3]. Combined cycles were investigated with ejector set at the absorber inlet [4–9]. *COP* of such cycles are reported to be higher by about 2–4% than that of conventional cycles. Principally, investigations indicate that *COP* of the combined configuration are greater or equal to that of single-effect cycles, but reached at lower generator temperatures.

Other configurations are discussed where the ejector is located at the condenser inlet of single-effect systems [10–14]. Theoretical investigations confirm the improvement of the performances in comparison with basic single-effect cycles. Experimental studies [15] show that this combined cycle is 30-60% more performant than conventional absorption cycles and almost reaches the *COP* of double-effect systems. Besides modifying configurations, adding a flash tank between ejector and evaporator was also proposed [16, 17].

Ejector improved double-effect absorption system was also investigated [18–20]. The *COP* of the proposed refrigeration scheme was found to increase with the temperature of the heat source until this temperature reaches 150°C. Beyond that value, the new cycle worked as a conventional double-effect cycle. Another configuration was studied with an ejector coupled to vapor generator [21–23]. This procedure is intended to enhance the concentration process by compressing the vapor produced from the lithium bromide solution in order to reheat the solution from which it came. Results showed that *COP* of the new cycle increases especially with the heat source temperature.

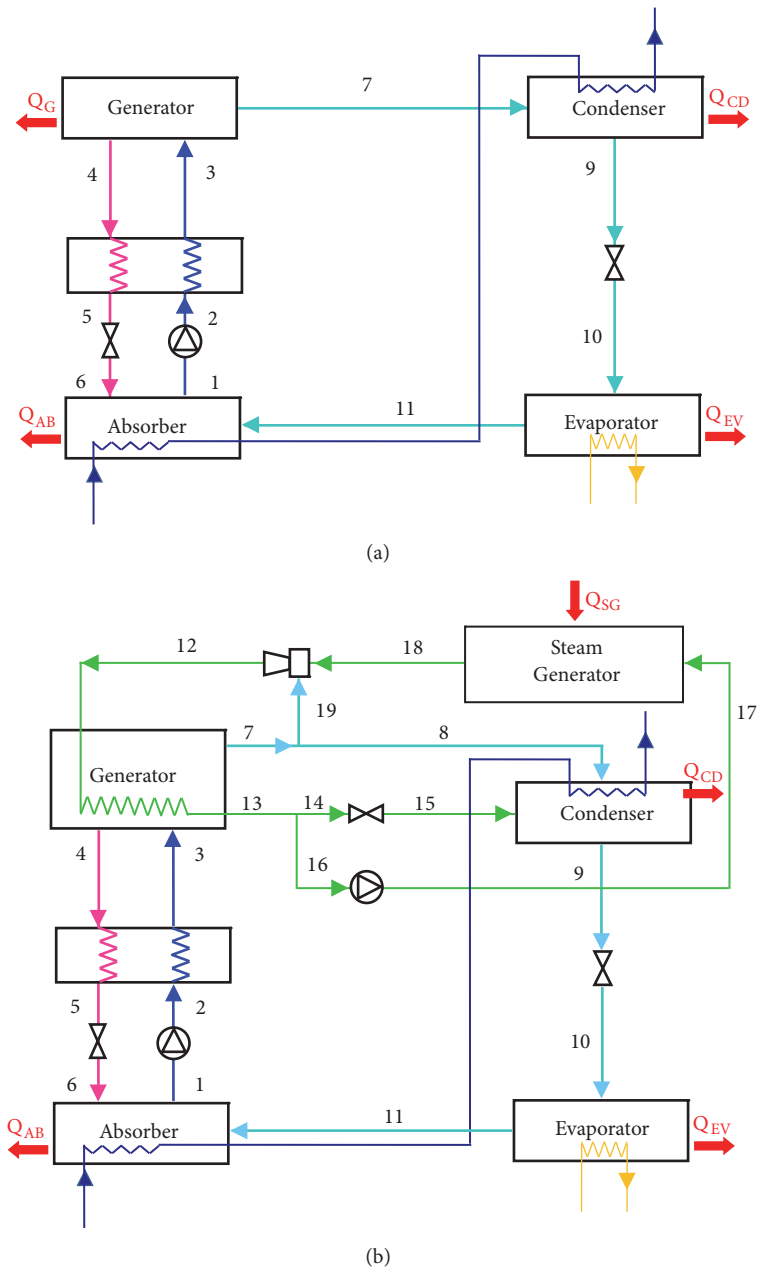

Figure 1: Single-effect absorption system: (a) conventional; (b) hybrid, ejector-enhanced.

In this paper, an ejector-activated single-effect LiBr-water cycle is proposed and theoretically investigated. The objective is to assess the feasibility and limits of performance of this new cycle scheme. If the *COP* of the proposed system could reach that of a conventional double-effect cycle, this would mean obtaining high performance by avoiding the configuration complexity of double-effect cycles. We investigate the evolution of the *COP* of the hybrid cycle with the steam generator temperature and the main factors of the cooling machine, i.e., desorber, condenser, and evaporator temperature. The behavior of the entrainment ratio as ejector performance criterion is also investigated for various primary and secondary flow pressure and backpressure.

2. System Description

Figures 1(a) and 1(b) are schematics of a conventional single-effect absorption cycle and an ejector-enhanced single-effect absorption system. A conventional single-effect absorption chiller (Figure 1(a)) is composed of evaporator, absorber, condenser, generator, solution expansion-valve, pump, solution heat exchanger, and refrigerant expansion-valve. In a hybrid system (Figure 1(b)) a steam-generator-ejector loop is coupled to the conventional single-effect installation via the machine generator. This extra circuit is constituted of an ejector, a steam generator, a water pump, and an expansion valve.

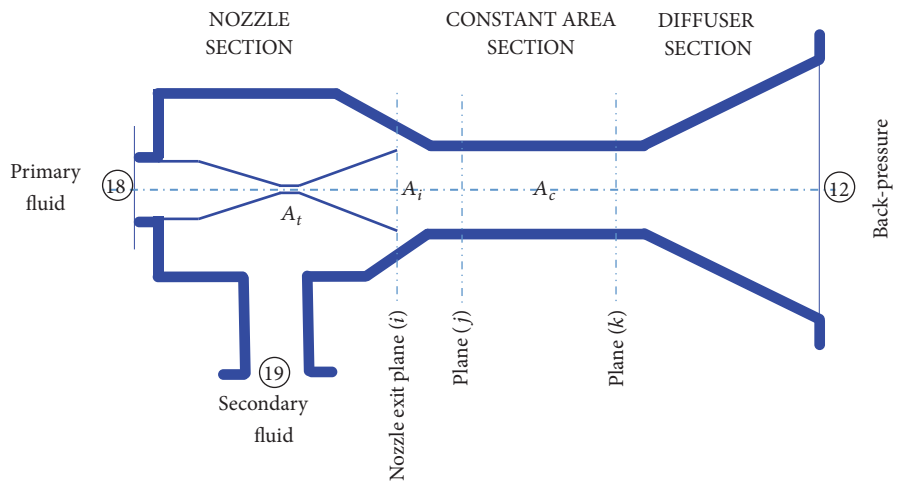

Figure 2: Ejector schematics.

The ejector loop is intended to improve the cycle performance by enhancing the concentration process in the machine generator. A high-pressure flow (18) coming from the external steam generator enters the primary nozzle of the ejector where its pressure drops while it is accelerated. At the nozzle exit section (i) (Figure 2) its velocity becomes supersonic and high enough to entrain a secondary flow (19 in Figure 1), part of the vapor (7) generated in the desorber. The two streams mix in the mixing chamber and the resulting gas, after undergoing a shockwave that reduces its velocity to subsonic, is compressed in the diffuser forming the last segment of the ejector. The exiting vapor (12) condenses in the coil placed inside the solution generator, liberating thus condensation heat used to concentrate the saline solution by desorbing vapor from the water-rich solution (3) entering the generator. Part of the condensate flows, after appropriate pressure reduction, to the condenser, and the rest is pumped back to the steam generator.

3. Chiller Model

Basing on mass and energy balances written for every machine element a mathematical model of the installation is set up. For the numerical simulations, a computer code of the machine model is realized using the software *E*ngineering *E*quations *S*olver, *EES* [24].

The model is elaborated under the following assumptions:

(i) Steady state conditions

(ii) Negligible heat losses to the surroundings at generator, condenser, absorber, and evaporator

(iii) Negligible pressure losses in pipes and components

(iv) Saturated refrigerant exiting condenser and evaporator

(v) Isenthalpic flow in solution and refrigerant valves

(vi) Phase equilibrium between solution entering refrigerant generator and vapor leaving

(vii) Constant solution flow-rate leaving the absorber, specifically 2 kg/s

(viii) Heat exchanger effectiveness, $\varepsilon_{HX} = 80\%$

In the following major elements of the model are presented.

3.1. Ejector Loop. This loop includes steam generator, ejector, heating coil placed in solution generator, expansion valve, and water pump.

(i) Steam Generator

The mass and energy balances on steam generator write, respectively,

$$\dot{m}_{17} = \dot{m}_{18} \tag{1}$$

$$\dot{Q}_{SG} = \dot{m}_{17}\left(h_{18} - h_{17}\right) \tag{2}$$

The properties of exiting saturated vapor (18) are:

$$P_{SG} = P_{18} = P_{W-sat}\left(T_{18}\right) \tag{3}$$

$$h_{18} = h_{W-sat}\left(T_{18}, X_{18} = 1\right) \tag{4}$$

Further, $P_{17} = P_{18}$.

Properties with index W for water refer to pure water properties as given in steam tables.

(ii) Ejector

The ejector performance depends on the backpressure P_{bp}—the pressure of the exiting (supposed saturated) steam flowing in the heating coil—, the primary pressure, P_{18}, and the secondary pressure, P_{19}. The relations between the different pressures around the ejector are

$$P_{bp} = P_{13} = P_{W-sat}\left(T_{13}\right) \tag{5}$$

$$P_{19} = P_7 = P_8 \tag{6}$$

The mass balance for the ejector writes

$$\dot{m}_{12} = \dot{m}_{18} + \dot{m}_{19} = (1 + \omega)\,\dot{m}_{18} \tag{7}$$

where ω stands for the entrainment ratio

$$\omega = \frac{\dot{m}_{19}}{\dot{m}_{18}} \tag{8}$$

The enthalpy of exiting flow (12) can be deduced from the energy balance

$$h_{12} = \frac{h_{18} + \omega h_{19}}{1 + \omega} \tag{9}$$

(iii) Heating Coil

Assuming a difference of 5 K between the temperatures of the heat source and that of the refrigerant generator solution, we get

$$T_{13} = T_{12} = T_G + 5 = T_4 + 5 \tag{10}$$

$$h_{13} = h_{W-sat}\left(T_{13}, X_{13} = 0\right) \tag{11}$$

The mass balance writes

$$\dot{m}_{12} = \dot{m}_{13} \tag{12}$$

(iv) Water Pump

We suppose approximately isothermal pumping

$$T_{17} = T_{16} = T_{13} = T_{14} \tag{13}$$

The mass and energy balances write, successively,

$$\dot{m}_{17} = \dot{m}_{16} \tag{14}$$

$$h_{17} = h_{16} + \frac{\left(P_{17} - P_{16}\right)}{\rho_{17}} \tag{15}$$

where the term $[(P_{17}-P_{16})/\rho_{17}]$ in the last equation represents the specific pump work (kJ/kg), with $(\rho_{17} = \rho_W(T_{17}, P_{17}))$.

(v) Expansion Valve

The expansion is isenthalpic, *i.e.*,

$$h_{14} = h_{15} = h_{13} \tag{16}$$

$$\dot{m}_{14} = \dot{m}_{15} \tag{17}$$

3.2. Liquid Solution Loop. The absorber-generator loop comprises absorber, solution valve, solution pump, solution heat exchanger, and refrigerant generator.

(i) Refrigerant Generator

With ξ denoting the lithium bromide concentration in the liquid solution, the mass balances for this machine element write

$$\dot{m}_3 = \dot{m}_7 + \dot{m}_4 \tag{18}$$

$$\dot{m}_4\xi_4 = \dot{m}_3\xi_3 \tag{19}$$

Solving for $\dot{m}_7$ yields

$$\dot{m}_7 = \dot{m}_4 \frac{\xi_4 - \xi_3}{\xi_3} \tag{20}$$

For the energy balance we get

$$\dot{m}_4 h_4 + \dot{m}_7 h_7 = \dot{m}_3 h_3 + \dot{m}_{12}\left(h_{12} - h_{13}\right) \tag{21}$$

from which we deduce

$$\dot{m}_4 = \frac{\dot{m}_{12}\left(h_{12} - h_{13}\right) - \left(\dot{m}_7 h_7 - \dot{m}_3 h_3\right)}{h_4} \tag{22}$$

The properties of water-weak solution (4) exiting the generator are determined as follows:

$$P_G = P_{CD} = P_4 \tag{23}$$

$$\xi_4 = \xi_{SOL-sat}\left(T_G, P_G\right) \tag{24}$$

$$h_4 = h_{SOL-sat}\left(T_G, \xi_4\right) \tag{25}$$

For known solution temperature and pressure, the saturation concentration can be deduced from solution property relations. Following equations fix the properties of exiting vapor at (7)

$$P_7 = P_G \tag{26}$$

$$T_7 = T_{SOL-sat}\left(P_7, \xi_3\right) \tag{27}$$

$$h_7 = h_W\left(T_7, P_7\right) \tag{28}$$

(ii) Solution Heat Exchanger

Besides the trivial relations

$$\begin{aligned} P_5 &= P_4 \\ P_3 &= P_2 \end{aligned} \tag{29}$$

Mass and energy balance equations write

$$\begin{aligned} \xi_5 &= \xi_4 \\ \xi_3 &= \xi_2 \\ \dot{m}_3 &= \dot{m}_2 \\ \dot{m}_5 &= \dot{m}_4 \end{aligned} \tag{30}$$

$$h_3 = h_2 + \frac{\dot{m}_4}{\dot{m}_2}\left(h_4 - h_5\right) \tag{31}$$

Considering the heat exchanger effectiveness, ε_{HX}, we have the following further relations:

$$T_5 = \varepsilon_{HX} T_2 + \left(1 - \varepsilon_{HX}\right) T_4 \tag{32}$$

$$h_5 = h_{SOL-sat}\left(T_5, \xi_5\right) \tag{33}$$

$$h_3 = h_{SOL-sat}(\xi_3, T_3) \tag{34}$$

(iii) Solution Valve

Through the solution valve, the pressure is reduced from condenser to evaporator pressure. In addition to the usual mass balance-equations ($\xi_6 = \xi_5$) and ($\dot{m}_6 = \dot{m}_5$) we have the relations

$$h_6 = h_5 \tag{35}$$

$$T_6 = T_{SOL-sat}(\xi_4, h_6) \tag{36}$$

(iv) Solution Pump

Again, we have the trivial mass balances $\dot{m}_2 = \dot{m}_1$and $\xi_2 = \xi_1$. As for the water-pump, the pumping process is assumed isothermal ($T_2 = T_1$). During pumping, the enthalpy of the refrigerant-rich solution from absorber is increased by $[(P_2 - P_1)/\rho_2]$, with $[\rho_2 = \rho_{SOL-sat}(\xi_2, h_2)]$,

$$h_2 = h_1 + \frac{P_2 - P_1}{\rho_2} \tag{37}$$

(v) Absorber

Per definition, ($T_{AB} = T_1$) and ($P_{AB} = P_1$). For the liquid solution (1) exiting the absorber we get in addition to the mass and energy balance equations

$$\begin{aligned} \dot{m}_1 &= \dot{m}_6 + \dot{m}_{11} \\ \dot{m}_1\xi_1 &= \dot{m}_6\xi_6 \end{aligned} \tag{38}$$

$$\dot{Q}_{AB} = (\dot{m}_{11}h_{11} + \dot{m}_6 h_6) - \dot{m}_1 h_1 \tag{39}$$

The property relations are

$$\xi_1 = \xi_{SOL-sol}(P_1, T_1) \tag{40}$$

$$h_1 = h_{SOL-sat}(T_1, P_1) \tag{41}$$

3.3. Refrigerant Loop

(i) Condenser

Streams (8) and (15) flow in the condenser where they condensate. Condensing temperature and pressure are $T_{CD} = T_9$ and $P_{CD} = P_9$, respectively. The mass and energy balances around the condenser write

$$\dot{m}_9 = \dot{m}_8 + \dot{m}_{15} = \dot{m}_8 + \dot{m}_{19} = \dot{m}_7 \tag{42}$$

$$\dot{Q}_{CD} = \dot{m}_9 (h_8 - h_9) \tag{43}$$

Knowing the condensation temperature T_9, pressure P_9 as well as the enthalpy of exiting liquid can be deduced as

$$P_9 = P_{W-sat}(T_9) \tag{44}$$

$$h_9 = h_{W-sat}(T_9, X_9 = 0) \tag{45}$$

(ii) Refrigerant Expansion Valve

Liquid refrigerant (9) undergoes a pressure reduction before it enters the evaporator. Evaporation temperature and pressure are $T_{EV} = T_{11} = T_{10}$ and $P_{EV} = P_{10}$, respectively.

For fixed evaporator temperature T_{EV} and assuming saturated vapor at exit, we can write $P_{EV} = P_{W-sat}(T_{EV})$.

The mass and energy balances for the valve write

$$h_{10} = h_9 \tag{46}$$

$$\dot{m}_{10} = \dot{m}_9 \tag{47}$$

(iii) Evaporator

The evaporator equations are

$$\dot{Q}_{EV} = \dot{m}_{11}(h_{11} - h_{10}) \tag{48}$$

$$\begin{aligned} \dot{m}_{11} &= \dot{m}_{10} \\ h_{11} &= h_{W-sat}(T_{EV}, X_{11} = 1) \end{aligned} \tag{49}$$

The COP_{hybrid} of the proposed absorption system, when neglecting all pump work, can be expressed as

$$COP_{hybrid} = \frac{\dot{Q}_{EV}}{\dot{Q}_{SG}} \tag{50}$$

4. Ejector 1D Model and Analysis

Because the performances of the proposed cycle depend largely on ejector performances, a reliable ejector model is necessary for the cycle simulations. In this paper, the ejector is modelled basing on the 1D analyses in [25, 26].

In this type of model, it is assumed that

(i) primary fluid expands isentropically in nozzle, and the exiting flow compresses isentropically in diffuser

(ii) inlet velocities of primary and entrained fluids are insignificant

(iii) velocity of the compressed mixture at ejector outlet is neglected

(iv) mixing of primary and secondary fluids in the suction chamber occurs at constant pressure

(v) flow in ejector is adiabatic

Isentropic efficiencies are introduced in the model to account for eventual irreversibility in the expansion process in primary nozzle, (η_n), in the mixing process of primary and secondary flow in the mixing chamber, (η_m), and finally in the compression process in the diffuser, (η_d). For the numerical simulations we set $\eta_n = 0.95$, $\eta_d = 0.95$, and $\eta_m = 1$.

4.1. Primary Nozzle. In the nozzle, the primary vapor (18) expands and accelerates. The Mach number M_{18i} of the fluid at nozzle outlet plane (i), deduced from energy balance, writes

$$M_{18i} = \sqrt{\frac{2\eta_n}{\gamma - 1}\left(\left(\frac{P_{18}}{P_i}\right)^{(\gamma-1)/\gamma} - 1\right)} \tag{51}$$

In this equation, η_n is the isentropic nozzle efficiency, defined as the ratio between actual enthalpy change and enthalpy change undergone during an isentropic process.

The expression for (A_i/A_t) the area ratio at nozzle throat and outlet is

$$\frac{A_i}{A_t} = \sqrt{\frac{1}{M_{18i}^2}\left(\frac{2}{\gamma+1}\left(1 + \frac{\gamma-1}{2}M_{18i}^2\right)\right)^{(\gamma+1)/(\gamma-1)}} \tag{52}$$

4.2. Suction Chamber. Because $P_i < P_{19}$, the secondary fluid (19) expands in the suction chamber and is entrained by the high-speed primary flow. The Mach number M_{19i} of the entrained fluid at nozzle exit plane writes

$$M_{19i} = \sqrt{\frac{2}{\gamma - 1}\left(\left(\frac{P_{19}}{P_i}\right)^{(\gamma-1)/\gamma} - 1\right)} \tag{53}$$

4.3. Mixing Chamber. Here, primary and secondary fluids are mixed. The properties of the resulting stream at section (j) are deduced from continuity, momentum, and energy equations and expressed as function of the critical Mach number M_j^*,

$$M_j^* = \eta_m \frac{M_{18i}^* + \omega M_{19i}^* \sqrt{\tau}}{\sqrt{(1+\omega\tau)(1+\omega)}} \tag{54}$$

As can be noticed, the mixture M_j^* is written as a combination of critical Mach numbers of the original streams, M_{18i}^* and M_{19i}^*. τ in this equation stands for the temperature ratio of incoming streams (19) and (18):

$$\tau = \frac{T_{19}}{T_{18}} \tag{55}$$

The relationship between M and M^* at any point of the ejector is given by the equation

$$M = \sqrt{\frac{2M^{*2}}{(\gamma+1) - (\gamma-1)M^{*2}}} \tag{56}$$

By the end of the mixing chamber, a shock wave occurs at section (k). The flow changes from supersonic to subsonic conditions, producing simultaneously a sudden rise in the static pressure. The relation between the Mach number upstream and downstream of the shock wave is given by

$$M_k = \sqrt{\frac{2/(\gamma-1) + M_j^2}{(2\gamma/(\gamma-1))M_j^2 - 1}} \tag{57}$$

The corresponding pressure increase writes

$$\frac{P_k}{P_j} = \frac{M_j}{M_k}\sqrt{\frac{1 + (1/2)M_j^2(\gamma-1)}{1 + (1/2)M_k^2(\gamma-1)}} \tag{58}$$

4.4. Diffuser. The expression of the pressure lift in the diffuser is

$$\frac{P_{12}}{P_k} = \left(1 + \frac{1}{2}\eta_d M_k^2(\gamma-1)\right)^{\gamma/(\gamma-1)} \tag{59}$$

The ejector area ratio (A_t/A_c), *i.e.*, the ratio of nozzle throat area and diffuser constant area section, writes

$$\frac{A_t}{A_c} = \frac{P_{12}}{P_{18}}\left(\frac{P_k}{P_{12}}\right)^{1/\gamma} \cdot \sqrt{1 - \left(\frac{P_k}{P_{12}}\right)^{(\gamma-1)/\gamma}}\sqrt{\frac{1}{(1+\omega\tau)(1+\omega)}} \cdot \frac{\sqrt{(\gamma+1)/(\gamma-1)}}{(2/(\gamma+1))^{1/(\gamma-1)}} \tag{60}$$

5. Results and Discussion

The *EES* machine model program is run to thermodynamically analyze the proposed hybrid single-effect absorption refrigeration system. The thermophysical properties of LiBr-H2O solution are estimated using the software property data- and model-bank.

The simulations are performed for the conditions given in Table 1. Evaporator temperature T_G is set to 4°C, condenser temperature T_{CD} to 37°C, and absorber temperature T_{AB} to $(T_{CD} - 2)$. Condenser and absorber are both supposed water-cooled. The cooling medium is processed thereafter in a cooling tower.

5.1. Program and Machine Model Validation. The simulation program is first validated by comparing our simulation results for a conventional single-effect cycle with the results published by Somers (2009) [27] for the same operating conditions: evaporator temperature,1.3°C; condenser and absorber temperatures at 40.2°C and 32.7°C, respectively; effectiveness of solution heat exchanger, 0.5; mass flow rate of solution leaving absorber, 1 kg/s. As can be noticed when comparing the results in columns 2 and 3 of Table 2, both sets of data are in very good agreement. Therefore, we can now proceed to the simulations of the proposed hybrid cycle with some confidence.

The next step was to validate the adequacy of the conventional model by comparing the predicted, calculated performance with experimental data reported in [28] concerning a large capacity LiBr-chiller. Two different sets of operating conditions are considered. As can be observed when studying columns 4 to 7 in Table 2, the calculated data is for both tests very close to the reported data in [28]. Finally, the proposed ejector configuration model is validated using

Table 1: Simulation input data.

Parameter	Value	Variation range
Steam generator pressure, P_{SG}, bar	15	10–15
Generator temperature, T_G, °C	80	65–90
Evaporator temperature, T_{EV}, °C	4	2–12
Condensation temperature, T_{CD}, °C	37	28–37
Absorber temperature, T_{AB}, °C	$T_{CD} - 2$	

Table 2: Program and machine model validation.

	Data 1 [27]	Present work	Data 2 [28]	Present work	Data 3 [28]	Present work
T_G, °C	90		101.6		83	
T_{EV}, °C	1.3		5		12.3	
T_{CD}, °C	40.2		43		42	
T_{AB}, °C	32.7		38.3		39	
$\dot{Q}_G$, kW	14.95	15.00	1150	1143	1100	1105
$\dot{Q}_{EV}$, kW	10.77	10.80	843	842.5	842.7	842.5
COP	0.73	0.72	0.73	0.74	0.76	0.76
ξ_4, %	62.6	62	65.5	65.8	57.2	58.5
ξ_3, %	57.4	56.3	56.5	57.4	53.1	53.4

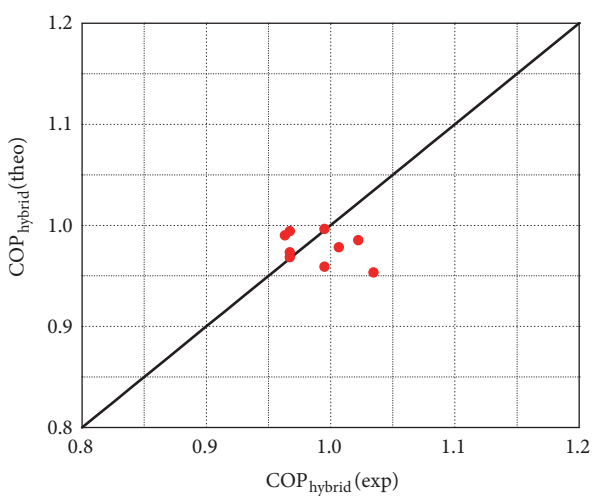

Figure 3: Hybrid cycle model validation basing on experimental data of ref. [29].

the only available experimental data found in the literature [29]. As represented in Figure 3, a fair agreement between calculated and reported data is noticed. Discrepancy may have its source in inaccuracy of experimental and/or too simple ejector model (ideal gas behavior).

5.2. Comparison of Hybrid and Conventional Cycle Performances. For purpose of illustration, the chiller cycle is represented in Figure 4 in the usual Oldham-diagram and in the water $(P - h)$–diagram in Figure 5.

We now proceed to the comparison of the performances of the proposed cycle and the conventional basic cycle (without ejector) for varying machine generator called also desorber-temperature (Figure 6), condenser temperature (Figure 7), and evaporator temperature (Figure 8).

As depicted in Figures 6–8, the coefficient of performance of the hybrid cycle is in all cases larger than the COP of the conventional cycle for the same operating conditions.

However, this performance enhancement is restricted to a specific interval of machine-generator temperature, as Figure 6 clearly shows. Outside this temperature interval, both cycles are practically equivalent. Figure 6 shows also that with growing desorber temperature T_G the COP–curve of the hybrid cycle first exceeds that of the basic cycle, reaches a maximum than decreases gradually, and resumes the curve of the conventional cycle COP. It is also worth noticing that the COP of the hybrid cycle under optimal conditions approaches the COP of double-effect conventional cycle.

Figures 7 and 8 depict the evolution of the COP of both cycles with condenser and evaporator temperature, respectively, for ($P_{18} = 15$ bar; $T_{18} \approx 200$°C). Note that T_{18} is the steam generator temperature, not the chiller desorber temperature, the abscissa in Figures 6–14. Both COP are expectably decreasing in the first case and increasing in the second. COP_{hybrid} is always larger than COP of conventional cycle because the constant maintained desorber-temperature is set to 80°C, *i.e.*, in the favourable interval 70°C–90°C. In conclusion of this section we notice that an ejector incorporated in the hybrid cycle (*i*) improves the cycle performances and (*ii*) the maximal COP is reached at lower machine generator temperature.

5.3. Performances of the Hybrid Cycle. The effect observed previously in Figure 6 (enhancement of the cycle performance due to the incorporation of ejector in the driving

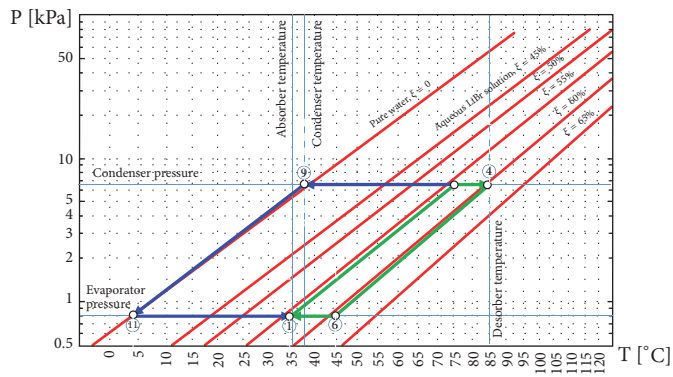

Figure 4: Chiller cycle representation in the Oldham-diagram ($T_{SG} \approx 200^{\circ}$C; $T_G = 85^{\circ}$C; $T_{EV} = 4^{\circ}$C; $T_{CD} = 37^{\circ}$C).

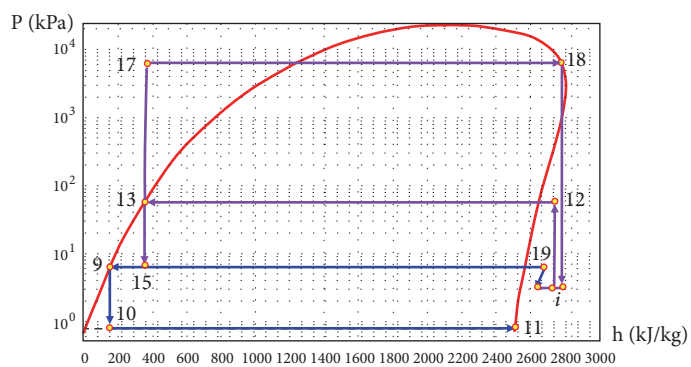

Figure 5: Chiller cycle representation in the water $(P - h)$–diagram ($T_{SG} \approx 200^{\circ}$C; $T_G = 85^{\circ}$C; $T_{EV} = 4^{\circ}$C; $T_{CD} = 37^{\circ}$C).

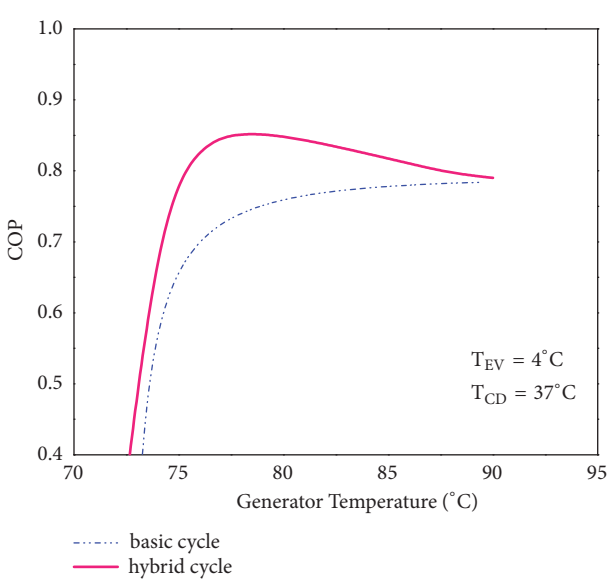

Figure 6: *COP* of hybrid and conventional cycle *vs.* machine generator temperature, $T_G(P_{18} = 15$ bar; $T_{18} \approx 200^{\circ}$C).

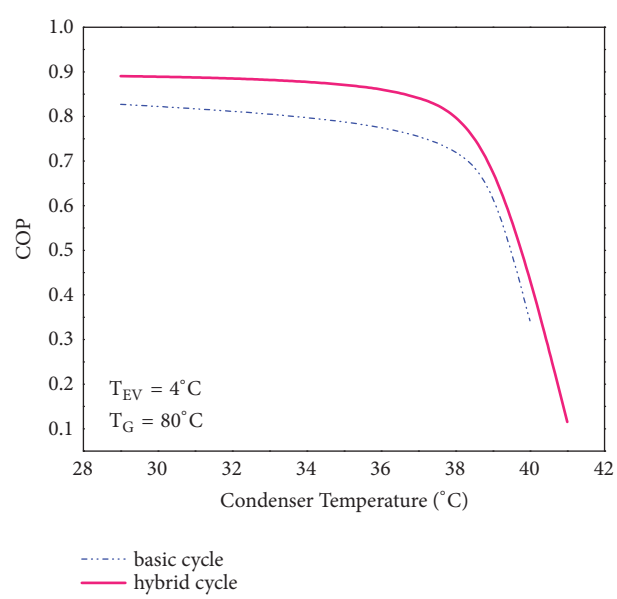

Figure 7: *COP* of hybrid and conventional cycle *vs.* condenser temperature, T_{CD}.

compartment of the machine) depends on the primary flow pressure $P_{SG} = P_{18}$ used to activate the ejector. Increasing this pressure expands this effect in magnitude and amplitude as Figure 9 shows: the higher the steam-generator pressure (and consequently temperature), the larger the machine-generator temperature range where the cycle performance is improved, and the higher the maximum *COP* that could

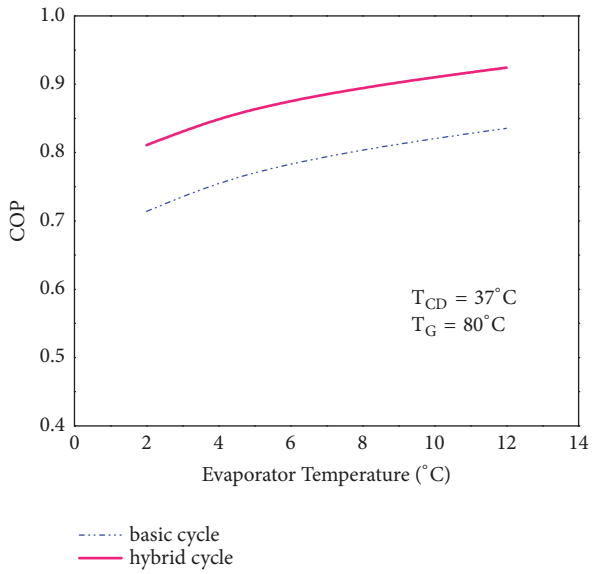

FIGURE 8: *COP* of hybrid and conventional cycle *vs.* evaporator temperature, T_{EV}.

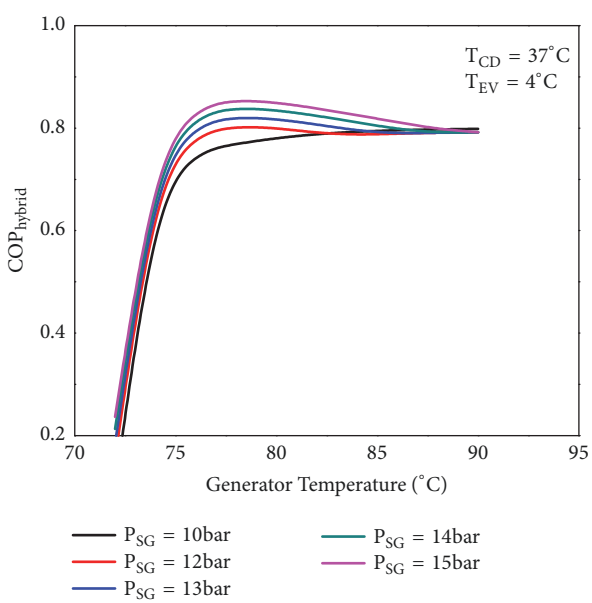

FIGURE 9: COP_{hybrid} *vs.* T_G for various steam-generator temperatures, T_{SG}.

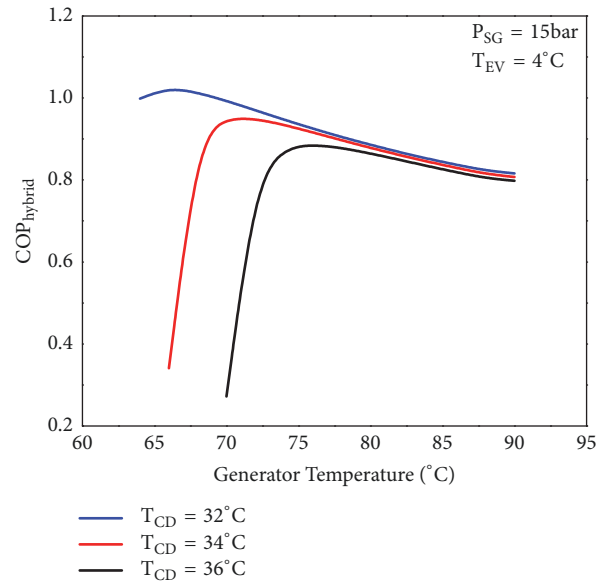

FIGURE 10: COP_{hybrid} *vs.* T_G for varying condenser temperature, T_{CD}.

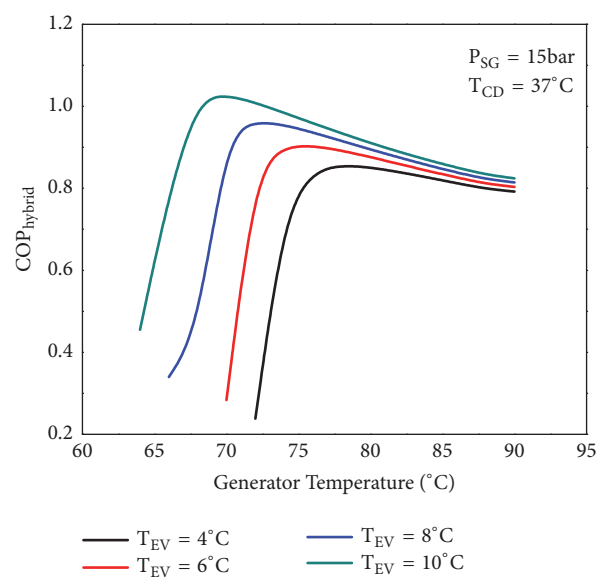

FIGURE 11: COP_{hybrid} *vs.* T_G for varying evaporator temperature, T_{EV}.

be reached inside this interval. On the opposite, when the steam generator pressure P_{SG} is decreased to 10 bar, practically no improvement more of the cycle performance is observed under the prevailing conditions.

Figure 10 depicts the evolution of COP_{hybrid} with T_G by varying the condenser temperature, T_{CD}. It is observed that the typical pink curve of Figure 6 is expectedly shifted to lower machine-generator temperatures (with lower condenser temperature, less high desorber temperature is needed to activate the cycle) with however concomitantly increased maximal *COP* and enlarged favorable temperature interval, where the cycle performance is improved.

Similar effects are observed in Figure 11 depicting the evolution of COP_{hybrid} with T_G by varying evaporator temperature. Here, the typical *COP*—improved portion of the curve is shifted to lower T_G—values when the evaporator temperature is *increased*, a thermodynamically more favourable situation. The *COP* of the hybrid cycle rises from 0.85 to 1.12 for generator temperature decreasing from 78°C to 67°C when the evaporator temperature increases from 4°C to 12°C.

5.4. Ejector Performance. The ejector model presented in Section 4 will help us interpret the represented simulation results in Figures 7–11 and assess the beneficial effect—and

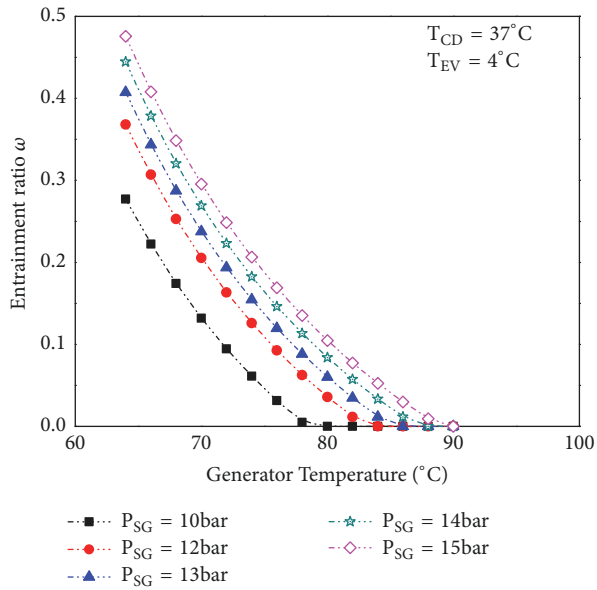

FIGURE 12: ω *vs.* T_G for various primary pressure P_{SG}.

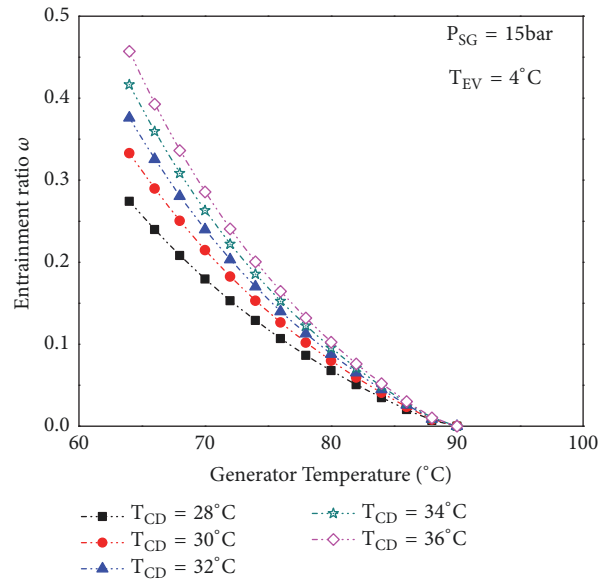

FIGURE 13: ω *vs.* T_G for various condenser temperature T_{CD}.

limits—of integration of an external ejector loop to a conventional absorption cycle. We first investigate the relation between the performance of the incorporated ejector, *i.e.*, its entrainment ratio ω, and significant absorption machine parameters, namely, desorber temperature T_G, evaporator temperature T_{EV}, and condenser temperature T_{CD}. Figure 12 depicts the evolution of ω with T_G. For a given primary pressure P_{SG}, the entrainment ratio decreases monotonously with T_G and finally vanishes for a maximal value of the desorber temperature; *i.e.*, secondary flow (19) is no more entrained inside the ejector. The ejector is then off-design and its geometry should be changed. Same behaviour of ω *vs.* T_G is noticed if the steam pressure P_{SG} is increased. However, in this case the curve is shifted upwards to larger values of ω; *i.e.*, more secondary vapour is sucked in the ejector for a given temperature T_G, and the limit value of T_G where the entrainment ration vanishes is pushed farther away.

Similar behaviour is observed in Figure 13, when for fixed primary pressure the condenser temperature (secondary pressure) is varied. If the condensation temperature is reduced (or alternatively enlarged), the entrainment ratio is also decreased (or increased, respectively). However, the curves ω *vs.* T_G for the various condenser temperatures all converge to the same point on the temperature-axis where ω vanishes. This temperature depends solely on the primary steam pressure.

Finally, Figure 14 shows that the evaporator temperature has practically no effect on the ejector performance by fixed P_{SG} and T_{CD}, as all ω *vs.* T_G for the various tested T_{EV} are superimposed.

According to the ejector model presented in Section 3 of the present paper, the entrainment ratio depends on six independent parameters: nozzle area ratio, primary flow and secondary flow properties, and backpressure, *i.e.*, $\omega = f(A_i/A_t, P_{18}, T_{18}, P_{19}, T_{19}, P_{12})$. The results presented in the

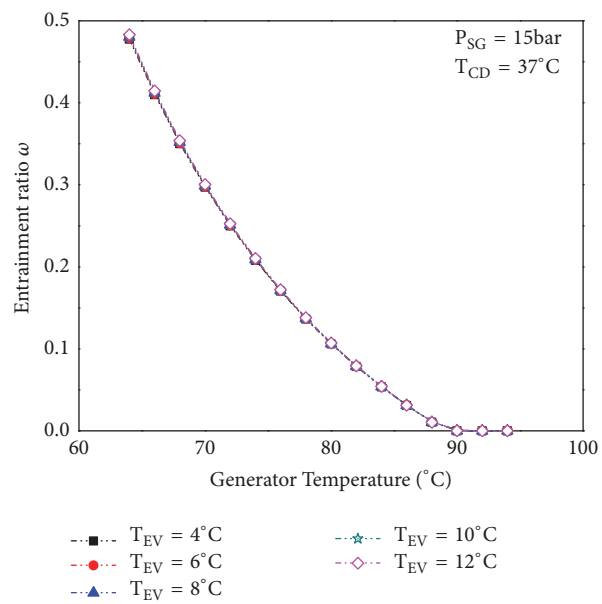

FIGURE 14: ω *vs.* T_G for various evaporator temperature T_{EV}.

foregoing sections are obtained for simulations with the specific conditions: (*i*) constant ejector nozzle ratio set to $(A_i/A_t) = 17.3$; (*ii*) saturated ejector-driving steam; *i.e.*, T_{18} and P_{18} are then no more both independent; (*iii*) pressure of secondary flow P_{19} equals condenser pressure, an independent parameter; (*iv*) temperature T_{19} of flow P_{19} is not an independent variable. It depends on the processes taking place in rest of the absorption chiller and in particular on the backpressure, P_{12}, which is considered here as an independent parameter.

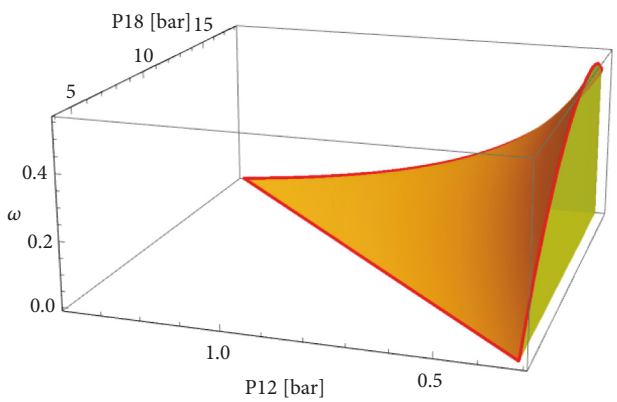

FIGURE 15: Entrainment ratio *vs.* primary pressure, P_{18}, and backpressure, P_{12}, for fixed nozzle area ratio, $(A_i/A_t) = 17.3$, and secondary pressure, $P_{19} = 0.0628$ bar.

In summary, the entrainment ratio depends then on just three parameters

$$\omega = f\left(P_{18}, P_{19}, P_{12}\right) \tag{61}$$

Figure 15 illustrates this dependency for a fixed secondary pressure, $P_{19} = 0.0628$ bar, as it is the case for the data depicted in Figures 6, 7, and 12. For a constant driving-steam pressure P_{18}, ω increases with falling backpressure, becomes a maximum, and decreases thereafter abruptly to zero. More generally, on increasing the ejector backpressure by fixed ejector geometry, a gradual reduction in entrainment ratio is induced. The maximal value of ω is the larger; *i.e.*, the greater the *COP*-improvement, the higher the P_{18}. Further, when P_{18} becomes larger, the interval of backpressure P_{12} (and hence, the range of T_{12} as well as the range of desorber temperature, T_4) where a chiller performance enhancement is expected, expands. The pressure difference $(P_{18} - P_{12})$ drives the ejector, and the difference $(P_{19} - P_i)$, where P_i is the pressure at nozzle exit, drives the entrainment process (Eq. (36)). With increasing primary pressure, P_i rises and comes closer to the secondary flow pressure P_{19}. The suction of the secondary flow into the mixing chamber declines gradually and eventually vanishes for $P_i = P_{19}$. Consequently, at this limit reached for $P_{18} = 18$ bar, ω falls to zero. The vertical isobar-plane $P_{18} = 18$ bar sets a geometrical limit to the used nozzle design.

The $\omega = 0$ plane limits also the 3D surface of Figure 15. The calculations show that the Mach number M_j of the mixed stream is there equal to M_{18i}, the Mach number of the primary flow at nozzle exit; *i.e.*, the mixed gas mass flow rate reduces to that of the primary flow and practically no secondary gas is entrained. This constitutes a higher limit for the design of the ejector area ratio (A_t/A_c), which comes then very close to the nozzle area ratio, (A_t/A_i). The maximum value of ω is found for minimal values of backpressure. At the limit, the Mach number of mixed gas M_j is the lowest and equals that of the entrained secondary flow M_{19i}.

The *COP* curves represented in Figures 6–9 depict its evolution when the effects of both the ejector and the single-effect absorption chiller are combined. By increasing the backpressure and, consequently, the desorber temperature, the *COP* tends first to increase as it does for a conventional cycle. The entrainment ratio however is decreasing. The resulting outcome is then first an increase of *COP* and then a decrease after passing a maximum where opposed effects cancel each other.

6. Conclusion

A hybrid single-effect cycle with water lithium-bromide as working fluid and activated by a steam-ejector loop is proposed and theoretically investigated. Mathematical models of the hybrid cycle and the ejector are detailed. Results show that entrainment ratio of the ejector depends on activating-steam pressure, on condenser temperature, and only slightly on evaporator temperature. For a fixed steam pressure, the *COP* of the hybrid cycle first surpasses that of the corresponding conventional cycle when the desorber temperature is increased, passes by a maximum, and then resumes the performance of the basic cycle. The maximum *COP* of an ejector-activated cycle is obtained at lower temperatures than that of a conventional system and can reach that of a double-effect basic scheme. The span of machine generator temperature where the *COP* is enhanced depends on the primary ejector pressure: it is larger for higher pressure. The entrainment ratio of the ejector is found to increase with the steam pressure and to decrease with rising backpressure. However, the performance of the ejector is confined to a specific region of the parameter-surface. Outside this domain, the entrainment ratio vanishes and the ejector is off-design.

Nomenclature

A: Area
$AiAt$: Nozzle area ratio (A_i/A_t)
$AcAt$: Ejector area ratio (A_c/A_t)
COP: Coefficient of performance
h: Specific enthalpy (kJ/kg)
$\dot{m}$: Mass flow rate (kg/s)
M: Mach number
M^*: Critical Mach number
P: Pressure (bar)
$\dot{Q}$: Heat transfer rate (kW)
R: Universal gas constant (kJ/(kg K))
T: Temperature (°C)
$\dot{W}$: Work transfer rate (kW)
X: Steam quality

Greek Symbols

γ: Ratio of steam specific heats (C_p/C_v)
ε_{HX}: Heat exchanger effectiveness
η: Nozzle, mixing, and diffuser efficiency

ξ: LiBr concentration in solution (mass. %)
ρ: Density (kg/m^3)
τ: T_{19}/T_{18}
ω: Entrainment ratio ($\dot{m}_{19}/\dot{m}_{18}$).

Subscripts

AB: Absorber
bp: Backpressure
c: Constant section area (ejector)
CD: Condenser
d: Diffuser (ejector)
EV: Evaporator
G: Generator
i: Nozzle exit plane (ejector)
j: Plane in mixing chamber (ejector)
k: Shockwave plane
m: Mixing chamber (ejector)
n: Nozzle (ejector)
sat: Saturation
SOL: Solution
SG: Steam generator
W: Water
1–19: Referred state points.

Data Availability

The data used to support the findings of this study are available from the corresponding author upon request.

Conflicts of Interest

The authors declare that they have no conflicts of interest.

References

[1] G. Besagni, R. Mereu, and F. Inzoli, "Ejector refrigeration: A comprehensive review," *Renewable & Sustainable Energy Reviews*, vol. 53, pp. 373–407, 2016.

[2] G. Besagni, "Ejectors on the cutting edge: The past, the present and the perspective," *Energy*, vol. 170, pp. 998–1003, 2019.

[3] G. Besagni, R. Mereu, P. Chiesa, and F. Inzoli, "An Integrated Lumped Parameter-CFD approach for off-design ejector performance evaluation," *Energy Conversion and Management*, vol. 105, pp. 697–715, 2015.

[4] L. Shi, J. Yin, X. Wang, and M. Zhu, "Study on a new ejection–absorption heat transformer," *Applied Energy*, vol. 68, no. 2, pp. 161–171, 2001.

[5] A. Sözen and M. Özalp, "Performance improvement of absorption refrigeration system using triple-pressure-level," *Applied Thermal Engineering*, vol. 23, no. 13, pp. 1577–1593, 2003.

[6] C. Vereda, R. Ventas, A. Lecuona, and M. Venegas, "Study of an ejector-absorption refrigeration cycle with an adaptable ejector nozzle for different working conditions," *Applied Energy*, vol. 97, pp. 305–312, 2012.

[7] L. Garousi Farshi, A. Mosaffa, C. Infante Ferreira, and M. Rosen, "Thermodynamic analysis and comparison of combined ejector–absorption and single effect absorption refrigeration systems," *Applied Energy*, vol. 133, pp. 335–346, 2014.

[8] A. Khaliq, R. Kumar, and E. M. Mokheimer, "Investigation on a solar thermal power and ejector-absorption refrigeration system based on first and second law analyses," *Energy*, vol. 164, pp. 1030–1043, 2018.

[9] S. Yosaf and H. Ozcan, "Exergoeconomic investigation of flue gas driven ejector absorption power system integrated with PEM electrolyser for hydrogen generation," *Energy*, vol. 163, pp. 88–99, 2018.

[10] D.-W. Sun, I. W. Eames, and S. Aphornratana, "Evaluation of a novel combined ejector - Absorption refrigeration cycle - I: Computer simulation," *International Journal of Refrigeration*, vol. 19, no. 3, pp. 172–180, 1996.

[11] H. S. Majdi, "Performance evaluation of combined ejector LiBr/H2O absorption cooling cycle," *Case Studies in Thermal Engineering*, vol. 7, pp. 25–35, 2016.

[12] A. M. Abed, K. Sopian, M. Alghoul, H. S. Majadi, and A. N. Al-Shamani, "Experimental evaluation of single stage ejector-absorption cooling cycle under different design configurations," *Solar Energy*, vol. 155, pp. 130–141, 2017.

[13] E. Bellos and C. Tzivanidis, "Parametric analysis and optimization of a cooling system with ejector absorption chiller powered by solar parabolic trough collectors," *Energy Conversion and Management*, vol. 168, pp. 329–342, 2018.

[14] S. Toghyani, E. Afshari, and E. Baniasadi, "Performance evaluation of an integrated proton exchange membrane fuel cell system with ejector absorption refrigeration cycle," *Energy Conversion and Management*, vol. 185, pp. 666–677, 2019.

[15] S. Aphornratana and I. W. Eames, "Experimental investigation of a combined ejector-absorption refrigerator," *International Journal of Energy Research*, vol. 22, pp. 195–207, 1998.

[16] R. Sirwan, M. Alghoul, K. Sopian, Y. Ali, and J. Abdulateef, "Evaluation of adding flash tank to solar combined ejector–absorption refrigeration system," *Solar Energy*, vol. 91, pp. 283–296, 2013.

[17] A. M. Abed, M. Alghoul, R. Sirawn, A. N. Al-Shamani, and K. Sopian, "Performance enhancement of ejector–absorption cooling cycle by re-arrangement of solution streamlines and adding RHE," *Applied Thermal Engineering*, vol. 77, pp. 65–75, 2015.

[18] D. Hong, G. Chen, L. Tang, and Y. He, "A novel ejector-absorption combined refrigeration cycle," *International Journal of Refrigeration*, vol. 34, no. 7, pp. 1596–1603, 2011.

[19] L. G. Farshi, S. S. Mahmoudi, M. A. Rosen, and M. Yari, "Use of low-grade heat sources in combined ejector–double effect absorption refrigeration systems," *Journal of Power and Energy*, vol. 226, no. 5, pp. 607–622, 2012.

[20] Y. Shi, F. Li, D. Hong, Q. Wang, and G. Chen, "Experimental study of a new ejector-absorption refrigeration cycle driven by multi-heat sources," *Applied Thermal Engineering*, vol. 133, pp. 604–612, 2018.

[21] I. W. Eames and S. Wu, "A theoretical study of an innovative ejector powered absorption–recompression cycle refrigerator," *International Journal of Refrigeration*, vol. 23, no. 6, pp. 475–484, 2000.

[22] D. Sioud, M. Bourouis, and A. Bellagi, "Investigation of an ejector powered double-effect absorption/recompression refrigeration cycle," *International Journal of Refrigeration*, vol. 99, pp. 453–468, 2019.

[23] D. Sioud, R. Garma, and A. Bellagi, "Thermodynamic analysis of a solar combined ejector absorption cooling system," *Journal of Engineering*, vol. 2018, pp. 1–12, 2018.

[24] F. Klein and S. A. Alvarado, "Engineering equation solver," Middleton, WI: F–chart software.

[25] H. El-Dessouky, H. Ettouney, I. Alatiqi, and G. Al-Nuwaibit, "Evaluation of steam jet ejectors," *Chemical Engineering and Processing: Process Intensification*, vol. 41, no. 6, pp. 551–561, 2002.

[26] B. Huang, J. Chang, C. Wang, and V. Petrenko, "A 1-D analysis of ejector performance," *International Journal of Refrigeration*, vol. 22, no. 5, pp. 354–364, 1999.

[27] C. Somers, *Modelling absorption chillers in Aspen.Simulation of absorption cycles for integration into refining processes [Masters of Science]*, University of Maryland, College Park, MD, USA, 2009, https://scholar.google.com/scholar_lookup?title=Modelling%20Absorption%20Chillers%20in%20aspen%2C%20%E2%80%9CSimulation%20of%20Absorption%20Cycles%20For%20Integration%20Into%20Refining%20processes%E2%80%9D&author=C.%20Somers&publication_year=2009.

[28] M. L. Chougui, *Simulation et étude comparée de cycle à absorption (LiBr/H2O) à usage de froid. Cas de l'unité de production de Henkel [Master]*, Université Mentouri, Constantine-Algérie, 2010, https://scholar.google.com/scholar?hl=en&as_sdt=0%2C5&q=Simulation+et+%C3%A9tude+compar%C3%A9e+de+cycle+%C3%A0+absorption+%28LiBr%2FH2O%29+%C3%A0+usage+de+froid.+Cas+de+l%E2%80%99unit%C3%A9+de+production+de+Henkel&btnG=.

[29] I. W. Eames and S. Wu, "Experimental proof-of-concept testing of an innovative heat-powered vapour recompression–absorption refrigerator cycle," *Applied Thermal Engineering*, vol. 20, no. 8, pp. 721–736, 2000.

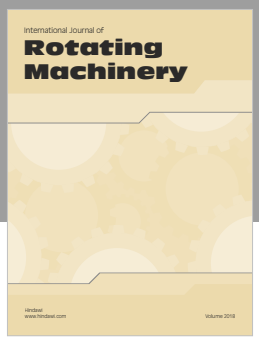

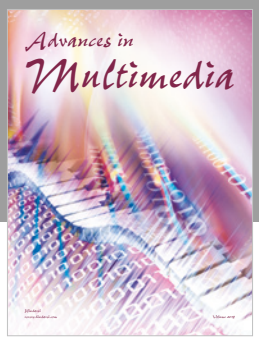

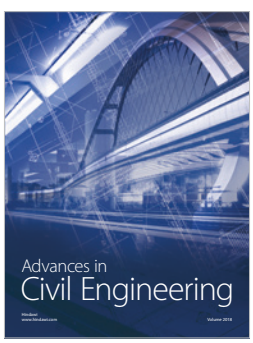

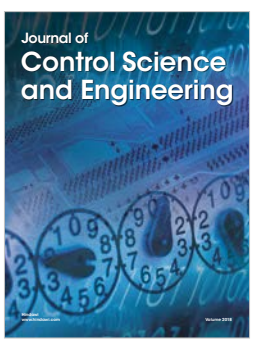

Hindawi

Submit your manuscripts at
www.hindawi.com